ÉCOLE POLYTECHNIQUE FÉDÉRALE DE LAUSANNE
MATHICSE
Institute of Mathematics
School of Basic Sciences

MATHICSE Technical Report
Nr. 05.2018
April 2018

Quantifying uncertainties in contact mechanics of rough surfaces using the Multilevel Monte Carlo method

Valentine Rey, Sebastian Krumscheid, Fabio Nobile

Address: EPFL - SB – INSTITUTE of MATHEMATICS – Math
(Bâtiment MA) Station 8 - CH-1015 - Lausanne - Switzerland

Quantifying uncertainties in contact mechanics of rough surfaces using the Multilevel Monte Carlo method

V. Rey[1,3], S. Krumscheid[2], F. Nobile[2]

[1]LSMS, Civil Engineering Institute, École Polytechnique Fédérale de Lausanne, 1015 Lausanne, Switzerland

[2] CSQI, Institute of Mathematics, École Polytechnique Fédérale de Lausanne, 1015 Lausanne, Switzerland

[3] GeM, UMR 6183 - University of Nantes, Centrale Nantes, BP 92208 - 44322 Nantes cedex 3,France

Abstract

We quantify the effect of uncertainties on quantities of interest related to contact mechanics of rough surfaces. Specifically, we consider the problem of frictionless non adhesive normal contact between two semi infinite linear elastic solids subject to uncertainties. These uncertainties may for example originate from an incomplete surface description. To account for surface uncertainties, we model a rough surface as a suitable Gaussian random field whose covariance function encodes the surface's roughness, which is experimentally measurable. Within this stochastic framework, we first introduce the complete random contact model, which includes the precise definition of the considered class of rough random surfaces as well as the study of a practical random surface generator. Then, we introduce the multilevel Monte Carlo method which is a computationally efficient sampling method for the computation of statistical moments of uncertain system output's, such as those derived from contact simulations. In particular, we consider two different quantities of interest, namely the contact area and the number of contact clusters, and show via numerical experiments that the multilevel Monte Carlo method offers significant computational gains compared to an approximation via a classic Monte Carlo sampling.

1 Introduction

Contact between interfaces is omnipresent in both nature and engineering applications, so that understanding the mechanical response to such contacts is a major scientific challenge of current interest. In fact, these contact problems can be found in virtually any engineering application characterized by interactions between separate parts and involving, for example, friction or wear.

Despite its fundamental importance, many aspects of contact mechanics remain poorly understood. One of the key challenges stems from the multiscale nature of the contact interfaces. Indeed, both natural and manufactured surfaces are not perfectly flat but are made of multiple asperities that exist at all length scales. The rough surfaces are usually modeled as semi-affine fractal surfaces [23], which are characterized through their height distribution (see [25] for experimental measurements). In spite of the fact that some surface properties can be measured, there remain uncertainties e.g. due to finite precision measurement and incomplete information. Therefore, surfaces are considered to be random and are usually characterized only through their statistical properties.

Describing the roughness of a surface via statistical properties for every engineering application would imply prohibitive computational costs, many numerical studies typically aim at considering semi-infinite volume (bulk with a rough surface) and obtaining mechanical responses, which will afterwards be used in a macroscopic model. More precisely, for a surface defined by its statistical properties, the contact area or the number of contact clusters under an imposed pressure is computed and this result is then used for more advanced mechanical problems. For example, being able to know the morphology of contact clusters for some class of rough surfaces is of primary importance to be able to study sealing technologies [9], the adherence of tires on roads [22, 35], and reliability considerations for nano electromechanical systems (NEMS) and micro electromechanical systems (MEMS) appliances [8].

Despite its clear practical importance, a systematic and reliable quantification of uncertainties in contact mechanics is often disregarded in the relevant literature. Furthermore, even works that acknowledge model uncertainties (e.g. [30, 27, 29]) quantify their effects on a quantity of interest often in a somewhat ad-hoc way. Moreover, since the numerical studies are typically done on a finite size surface with periodic boundary conditions, an

error due to homogenization (with finite size of the representative surface element) is introduced. Consequently, a rational and effective quantification of uncertainties in contact simulations has not been introduced so far, a fact that further demonstrates the necessity of the present study.

In this paper, we will consider the frictionless non adhesive normal contact between one semi-infinite flat linear elastic solid and one semi-infinite rigid rough surface. To do so, we incorporate a stochastic modeling aspect by means of a class of appropriate random surfaces into well-established contact models. First, we define the contact problem on on a randomized semi-infinite surface (problem $\mathcal{P}$). Then, this problem is approximated by the truncation to a finite size surface with periodic boundary conditions, which gives the second problem $\mathcal{P}^L$. Finally, we present the third problem $\mathcal{P}_h^L$, which is the discretized version of $\mathcal{P}^L$ based on an integral formulation and Fourier approximation.

Since the contact problem is often computationally challenging due to the presence of multiple length scales, quantifying the effect of a random rough surface, by e.g. the classic Monte Carlo method, becomes quickly computationally prohibitive. Recently, the multilevel Monte Carlo (MLMC) method has been established as a computationally efficient sampling method that is applicable to a wide range of random models [13, 7, 34, 14, 26]. In this work, we will investigate the benefits of these multilevel Monte Carlo techniques applied to random rough contact mechanics problems, for which it will be key to carefully balance statistical errors and discretization errors. Our primary focus is on the effect of the discretization parameter h for a fixed, a priori chosen, truncation level L. In our numerical assessments, we have verified that the chosen finite domain size L has been taken sufficiently large so that the error due to finite box size does not dominate the discretization error. Somewhat related works that have applied the multilevel Monte Carlo method to a similar mechanical problem include [5, 3, 4]. In these works, simplified random obstacle problems governed by the Laplacian (i.e. ignoring elasticity) have been considered, for which the surface of the random obstacle is considered to be rough and given in terms of a Fourier cosine series with random shift, or with random shift and random amplitude. Recently, the MLMC method has also successfully been applied in the context of (stochastic) numerical homogenization of randomly heterogeneous material [10].

The rest of this paper is organized as follows. In Sect. 2 we introduce the deterministic contact mechanics model and its discretization, which is the basis of this work. Then, in Sect. 3, we introduce the random contact

model, which includes the definition of a class of suitable rough random surfaces and a description of how to sample these surfaces in practice. In Sect. 4 we introduce the multilevel Monte Carlo sampling technique, which is subsequently used in Sect. 5 to quantify uncertainties in quantities of interest derived from contact mechanics simulations. Finally, conclusions and an outlook on future works are offered in Sect. 6.

2 The deterministic mechanic contact model

In this section, we briefly describe the deterministic contact model and its discretization for a given surface. Specifically, we begin with a continuous model that is then approximated appropriately to yield a model that is amenable for computational treatment. As mentioned above, here we focus on the non-adhesive frictionless normal elastic contact. It is noteworthy that the deterministic model described below is not novel, but is standard and well-established in the literature [2, 37].

2.1 Semi-infinite continuous model

As initial idealized model (denoted by $\mathcal{P}$), we consider two semi-infinite continuous solids. The first solid is rigid (i.e. infinitely stiff) and rough, in the sense that this solid's surface is characterized by the presence of asperities on a wide range of length scales. In fact, the roughness of a surface can be described via its surface profile. We denote a surface's profile by $s\colon \mathbb{R}^2 \to \mathbb{R}$, so that every point on the surface can be written as $\big(\mathbf{x}, s(\mathbf{x})\big) \in \mathbb{R}^3$, $\mathbf{x} \in \mathbb{R}^2$. The second solid is assumed to be perfectly flat and deformable. Throughout this paper we will work under the small strain assumption and consider the solid's behavior to be linear homogeneous isotropic elastic. Furthermore, we denote the solid's Young's modulus by E and its Poisson ratio by ν.

A mathematically convenient representation of the contact problem is in terms of an integral representation; see, e.g., [6]. In fact, this integral formulation provides a representation in which the only unknown that needs to be determined is the normal displacement field of the elastic solid's surface when the two solids come into contact. The advantage of this formulation thus is a dimension reduction, since the problem becomes effectively two dimensional. Moreover, the displacement field inside the bulk material does not need to be resolved as it can simply be recovered from the displacement

field at the surface of the elastic solid; see [31] for details.

2.2 Truncated continuous model

The first approximation to the idealized semi-infinite model $\mathcal{P}$ is to truncate the domain of interest. That is, instead of considering the two solids as semi-infinite, we will consider both solids on a bounded domain. Specifically, we consider them on a square D, say, with edge length $L > 0$, i.e. $D = [0, L]^2 \subset \mathbb{R}^2$. The only unbounded direction is therefore the inward normal at the surface. To represent semi-infinite solids using the bounded domain D, we impose periodic boundary conditions (PBCs) on the displacement field on the boundary of D. The resulting model is denoted by $\mathcal{P}^L$. Notice that $\mathcal{P}^L$ is still a fully continuous contact model.

The link between the normal displacement $u\colon \mathbb{R}^2 \to \mathbb{R}$ and the normal pressure $p\colon \mathbb{R}^2 \to \mathbb{R}$ at the surface is given by

$$u = K * p \,. \tag{1}$$

Here, the kernel $K\colon \mathbb{R}^2 \to \mathbb{R}$ depends on the material properties E and ν as well as on the fundamental solution that is chosen in the integral formulation; see [6] for details. In order to formulate the contact problem, it is furthermore convenient to introduce the so-called gap function $g\colon \mathbb{R}^2 \to \mathbb{R}$ as the distance between the two contacting surfaces, so that $g = u - s$. The well-known Hertz–Signorini–Moreau orthogonality condition then characterizes the non-adhesive contact problem and reads:

$$p(\mathbf{x})g(\mathbf{x}) = 0 \,, \quad p(\mathbf{x}) \geq 0 \,, \quad g(\mathbf{x}) \geq 0 \quad \forall \mathbf{x} \in D \,. \tag{2}$$

In other words, the condition states that interpenetration is forbidden ($g(\mathbf{x}) \geq 0$), that contact pressure can only be compressive ($p(\mathbf{x}) \geq 0$), and that each point is either in contact with the rigid surface ($g(\mathbf{x}) = 0$) or free of forces ($p(\mathbf{x}) = 0$). For clarity, we give a schematic representation of the problem in Figure 1.

The mechanic contact problem depends on a non-negative prescribed loading $\bar{p}$, which is related to the average spatial pressure, in the sense that

$$\frac{1}{|D|} \int_D p(\mathbf{x}) \, d\mathbf{x} = \bar{p} \,. \tag{3}$$

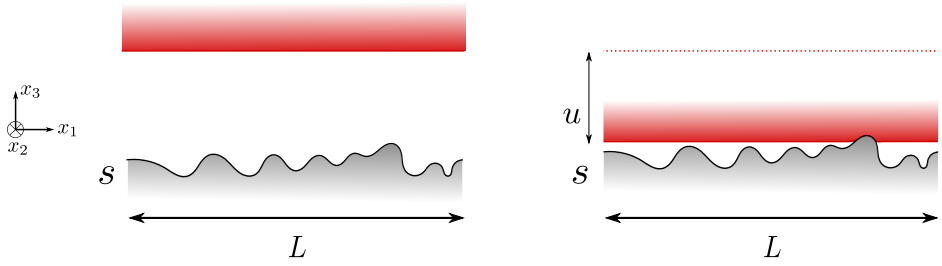

Figure 1: A 2-D sketch of two semi infinite solids coming into contact (2d view).

Combining everything together, problem $\mathcal{P}^L$ can be stated as:

$$\text{Find } p \in \mathcal{A} \text{ such that } E_c(p) \text{ is minimized.} \tag{4}$$

Here, E_c is the so-called complementary energy functional, which is given by

$$E_c(p) = \frac{1}{2}\int_D u(\mathbf{x})p(\mathbf{x})\,d\mathbf{x} - \int_D s(\mathbf{x})p(\mathbf{x})\,d\mathbf{x}\,, \tag{5}$$

and $\mathcal{A}$ denotes the space of admissible periodic pressure fields

$$\mathcal{A} \equiv \mathcal{A}(\bar{p}) := \left\{ p\colon D \to \mathbb{R} \text{ periodic such that } p \geq 0 \text{ and } \frac{1}{|D|}\int_D p(\mathbf{x})\,d\mathbf{x} = \bar{p} \right\}. \tag{6}$$

We reiterate that models $\mathcal{P}$ and $\mathcal{P}^L$ are not identical. In fact, there may be a model discrepancy due to the truncation of the domain and the PBCs. However, this model discrepancy vanishes as $L \to \infty$.

2.3 Discretization of the truncated model

The truncated continuous model $\mathcal{P}^L$ introduced above is amenable for further discretization to eventually provide a computational contact simulation tool. Specifically, we discretize the model $\mathcal{P}^L$ via the boundary element method (BEM) and denote the resulting model by $\mathcal{P}^L_h$.

To apply the BEM, we first introduce the spatial discretization parameter $h > 0$ that is used to construct a grid. Here we consider a uniform grid on the square domain D consisting of n^2 grid points (nodes), where $n \geq 2$ with $h = L/n$ (opposite edges are considered only once). An example of such

uniform grid is illustrated in Figure 3 (left). We represent both the surface of the flat deformable solid and the rough surface of the rigid solid on said grid by their nodal values to obtain discrete (i.e. finite dimensional) surface representations. Moreover, we denote by $\mathbf{u} \in \mathbb{R}^{n^2}$ the vector containing the n^2 nodal values of the displacement function u and, analogously, by $\mathbf{p} \in \mathbb{R}^{n^2}$ the vector containing the n^2 nodal values of the pressure p. That is, the component p_i (respectively u_i) of $\mathbf{p}$ (resp. $\mathbf{u}$) corresponds to the value of the pressure p (resp. the displacement u) at node i.

For the continuous model $\mathcal{P}^L$, equation (1) implies that $u = \mathcal{F}^{-1}\big(\mathcal{F}(K)\mathcal{F}(p)\big)$ in view of the convolution theorem for the Fourier transform $\mathcal{F}$. For the discrete case, we thus relate the displacement vector $\mathbf{u}$ and the elastic pressure vector $\mathbf{p}$ via

$$\mathbf{u} = \mathrm{FFT}^{\text{-}1}(\hat{\mathbf{K}}\,\mathrm{FFT}(\mathbf{p}))\,, \tag{7}$$

where FFT and FFT$^{\text{-}1}$ denote the 2D fast Fourier transform (2D-FFT) and the inverse 2D-FFT, respectively. Here we use the fast Fourier transform because of its efficiency, which is also one of the main reasons making the BEM appealing for contact problems. Moreover, note that the FFT implicitly enforces periodic boundary conditions on the surface, since displacements computed from (7) will be L-periodic. In equation (7), $\hat{\mathbf{K}} \in \mathbb{C}^{n^2 \times n^2}$ is a diagonal matrix that contains the so-called influence coefficients for the fundamental solution in Fourier space. Here, we use the Westergaard's reference solution [36]; see also [33] for the expression of the influence coefficients.

We note that the coefficient in the matrix $\hat{\mathbf{K}}$ associated to the mean value (i.e. the zero frequency) is set to zero. Indeed, the displacement of the surface is only known up to a rigid-body motion, since the problem is ill-posed in the x_3 direction. This choice will force $\mathbf{u}$ to have zero average, i.e. $\frac{1}{n^2}\sum_{i=1}^{n^2} u_i = 0$. Equivalently, one can, of course, also obtain a pressure from a displacement vector $\mathbf{u}$ using

$$\mathbf{p} = \mathrm{FFT}^{\text{-}1}(\hat{\mathbf{K}}^{-\mathbf{1}}\,\mathrm{FFT}(\mathbf{u})) + \bar{p}\,. \tag{8}$$

Here, we slightly abuse notation and assume that the coefficient of $\hat{\mathbf{K}}^{-\mathbf{1}}$ associated to the mean value (zero frequency) vanishes. Analogously to the continuous model, we then define the space of admissible (discrete) pressure vectors by

$$\boldsymbol{\mathcal{A}} \equiv \boldsymbol{\mathcal{A}}(\bar{p}) := \left\{ \mathbf{p} \in \mathbb{R}^{n^2},\ \mathbf{p}_i \geq 0 \,\middle|\, \frac{1}{n^2}\sum_{i=1}^{n^2} p_i = \bar{p} \right\}. \tag{9}$$

Eventually, the discrete problem $\mathcal{P}_h^L$ reads:

$$\text{Find } \mathbf{p} \in \boldsymbol{\mathcal{A}} \text{ such that } E_c(\mathbf{p}) \text{ is minimized,} \tag{10}$$

where the discrete complementary energy is

$$E_c(\mathbf{p}) = \frac{1}{2} \sum_{i=1}^{n^2} u_i p_i - \sum_{i=1}^{n^2} s_i p_i \ . \tag{11}$$

The minimization problem above is then solved using a constrained conjugate gradient approach; see, e.g., [28, 32]. Finally, we recall that model $\mathcal{P}_h^L$ is an approximation of model $\mathcal{P}^L$, so that solutions to these problems may differ due to the discretization error. However, this error vanished as h tends to zero [6].

3 The random contact model for rough surfaces

As mentioned in the introduction, both natural and manufactured surfaces are rough, in the sense of being composed of multiple asperities. In fact, experimental data indicate that surfaces are characterized by a wide range of length scales, from sample size to nanometer. To accurately model contact between two rough solids, one has to take this surface roughness into account because it can drastically affect a derived quantity of interest. For example, the true contact area is actually significantly smaller than the nominal contact area obtained when neglecting surface roughness. As moreover rough surfaces can usually not be determined fully within the entire domain of interest but are only given in terms of their statistical properties, a stochastic contact model is necessary to account for these uncertainties. To this end, we consider the deterministic contact models described in Sect. 2 for a class of random rough surfaces, which are modeled as Gaussian random fields. The considered class of surfaces is thereby defined via the surface's statistical description, e.g. by means of a characterization of its height distribution or of its power spectrum, which may be available through experimental results. As an illustration, Figure 2 shows the pressure distributions under a specific load $\bar{p} = 10$ and the two associated different realizations of a rough random surface. Each surface is one realization defined by the same fixed power spectrum. In what follows, we will describe the randomized contact model and discuss how to sample appropriate random surfaces that can then be used to produce the plots shown in Figure 2.

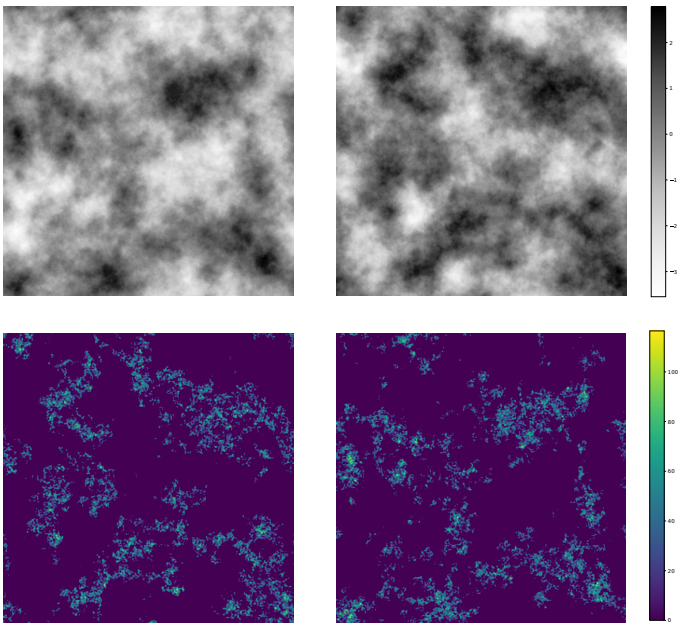

Figure 2: Typical pressure distributions (in color) obtained under a load $\bar{p} = 10$ corresponding to two different realizations of a rough random surface (in gray) defined by the same power spectrum.

3.1 Randomized contact models

As the rough surface is no longer deterministic but random, also the associated contact models $\mathcal{P}$, $\mathcal{P}^L$ and $\mathcal{P}_h^L$ are random. Specifically, let $(\Omega, \mathcal{F}, \mathbb{P})$ be a probability space. The random surface is then given by $s\colon \mathbb{R}^2 \times \Omega \to \mathbb{R}$, so that for any elementary random event $\omega \in \Omega$ the function $s(\cdot, \omega)$ is a surface profile as considered in Sect. 2. Consequently, the randomized counterparts of the deterministic contact models are simply given by replacing the fixed (i.e. deterministic) surface by a random one. In other words, a deterministic contact model can be thought of as a special case of its randomized counterpart, namely for just one specific surface realization. The randomized version

of problem $\mathcal{P}^L$ (denoted by $\mathcal{P}^L(\omega)$ to emphasize the stochastic nature) reads:

For (almost every) $\omega \in \Omega$, find $p(\cdot, \omega) \in \mathcal{A}$ such that

$$E_c\big(p(\cdot,\omega),\omega\big) = \frac{1}{2}\int_D u(\mathbf{x},\omega)p(\mathbf{x},\omega)\,d\mathbf{x} - \int_D s(\mathbf{x},\omega)p(\mathbf{x},\omega)\,d\mathbf{x} \tag{12}$$

is minimized,

where the *deterministic* set $\mathcal{A} \equiv \mathcal{A}(\bar{p})$ is as before. Similarly, the randomized fully discrete problem, i.e. $\mathcal{P}_h^L(\omega)$, reads:

For (almost every) $\omega \in \Omega$, find $\mathbf{p}(\omega) \in \boldsymbol{\mathcal{A}}$ such that

$$\text{the discrete complementary energy } E_c\big(\mathbf{p}(\omega),\omega\big) = \frac{1}{2}\sum_{i=1}^{n^2} u_i(\omega)p_i(\omega) - \sum_{i=1}^{n^2} s_i(\omega)p_i(\omega)$$

is minimized. (13)

It is worthwhile to emphasize here that the surface's randomness implies that also the solutions to the contact problems (as introduced above) are random, such as the displacement, the pressure, the gap function, and other derived quantities. For notational convenience, we will, however, often drop the dependency on $\omega \in \Omega$ and simply write $s(\mathbf{x})$ for a random surface for example.

3.2 A characterization of rough surfaces

In this subsection, we define the class of rough surfaces that we consider in this work. As mentioned in the introduction, we will use random fields [21]. Specifically, we model a random surface $s\colon D \times \Omega \to \mathbb{R}$ as an isotropic Gaussian random field with mean zero. That is, the m-dimensional random vector $\mathbf{s} := \big(s(\mathbf{x}_1), s(\mathbf{x}_2), \ldots, s(\mathbf{x}_m)\big)^T$ follows a multivariate Gaussian distribution for any $\mathbf{x}_1, \ldots, \mathbf{x}_m \in D$ and any $m \in \mathbb{N}$. Specifically, $\mathbf{s} \sim \mathcal{N}_m(\mathbf{0}, \Sigma)$ where the entries $\Sigma_{i,j}$ of the covariance matrix Σ are given by

$$\Sigma_{i,j} = c\big(|\mathbf{x}_i - \mathbf{x}_j|\big) \equiv \mathrm{Cov}\big(s(\mathbf{x}_i), s(\mathbf{x}_j)\big)\ . \tag{14}$$

Here, the function $c\colon \mathbb{R}^+ \to \mathbb{R}$ is called isotropic covariance, which only depends on the euclidean norm $r := |\mathbf{x}|$ of any point $\mathbf{x} \in \mathbb{R}^2$. Notice that

the isotropy also implies the stationarity of the field s. From the Wiener–Khinchin theorem it follows that the (power) spectral density Φ of the stationary Gaussian field s is given as the Fourier transform of its covariance function, in the sense that $\Phi(\mathbf{k}) = \frac{1}{4\pi^2}\int_{\mathbb{R}^2} e^{-i\mathbf{k}\cdot\mathbf{x}} c(\mathbf{x})\, d\mathbf{x}$. Furthermore, the isotropy of s implies that the spectral density only depends on the euclidean norm $k := |\mathbf{k}|$ of any Fourier point $\mathbf{k} \in \mathbb{R}^2$. That is, in our setting we have that $\Phi_r \colon \mathbb{R}^+ \to \mathbb{R}$, which is sometimes called radial spectral density. Moreover, its link to the isotropic covariance c is given by:

$$c(r) = 2\pi \int_0^\infty \Phi_r(k) J_0(kr) k \, dk \;, \tag{15}$$

where $J_0(kr)$ is the Bessel function of first kind [1].

The reason for expressing the isotropic covariance c in terms of the spectral density Φ is that identity (15) is particularly convenient when modeling rough surfaces. In fact, experimental results [25] suggest that rough surfaces can be characterized by a (radial power) spectral density Φ_r of the form

$$\Phi_r\big(|\mathbf{k}|\big) = \begin{cases} C & \text{, if } k_l \le |\mathbf{k}| \le k_r \;, \\ C\Big(\frac{|\mathbf{k}|}{k_r}\Big)^{-2-2H} & \text{, if } k_r \le |\mathbf{k}| \le k_s \;, \\ 0 & \text{, otherwise.} \end{cases} \tag{16}$$

Here, $H \in [0,1]$ denotes the Hurst exponent, $C \ge 0$ is the roughness amplitude, and the wave numbers $0 \le k_l \le k_r \le k_s$ control the different roughness regimes. Using identity (15), we can thus express the surface's variance $c(0)$ with respect to these parameters:

$$c(0) = \pi C \left(\frac{k_r^{-2H} - k_s^{-2H}}{H k_r^{-2-2H}} + k_r^2 - k_l^2 \right) \;. \tag{17}$$

From the wave numbers controlling the different regimes, one can, as is common practice, define the associated wave lengths $\lambda_l = \frac{2\pi}{k_l}$, $\lambda_s = \frac{2\pi}{k_s}$ and $\lambda_r = \frac{2\pi}{k_r}$.

3.3 Generating random rough surfaces on a grid

To solve the randomized discrete contact model $\mathcal{P}_h^L(\omega)$ (see Sect. 3.1) it is necessary to generate samples (i.e. realizations) of a random surface on

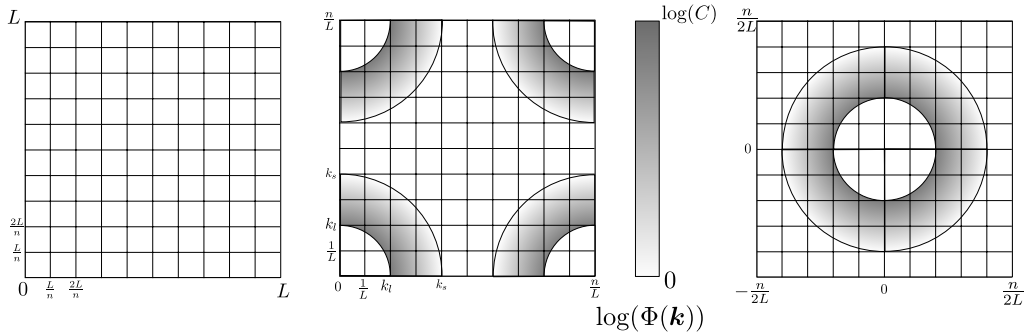

Figure 3: Spatial (left) and frequential (center and right) grids used for the generation and the representation of the rough surface.

a specific spatial grid. Specifically, it is required to generate independent random surface realizations that are isotropic Gaussian random fields with mean zero and prescribed covariance structure. In this section, we discuss how to generate such a (discretized) rough surface on the domain $D = [0, L]^2$. Moreover, we verify that the used sampling routine does indeed produce samples with the desired statistical properties.

In view of the periodicity inherent in the truncated problem $\mathcal{P}^L(\omega)$ and its discretization $\mathcal{P}_h^L(\omega)$, it is natural to also generate random surfaces that are periodic. That is, instead of generating samples of a random field with, for example, given isotropic covariance c (see Eq. (15)), here it is desired to use a periodic version of that covariance. For that purpose, let us denote by $\widetilde{c} : \mathbb{R}^2 \to \mathbb{R}$ the L-periodic version of the surface's isotropic covariance c given by $\widetilde{c}(\mathbf{x}) = \sum_{\mathbf{z}\in\mathbb{Z}^2} c(|\mathbf{x}+L\mathbf{z}|)$ and by $\widetilde{\Phi}_r$ the 2D power spectral density associated to $\widetilde{c}$ so that (15) formally holds for $\widetilde{c}$ and $\widetilde{\Phi}_r$. For the discretizations of both the spatial and the frequential domain considered here (see Fig. 3), it follows that $\widetilde{\Phi}_r$ is a sum of Dirac deltas located in the frequency grid points. In fact, in Figure 3 (center) we illustrate the frequential grid used to discretize a power spectrum density Φ, which is also sketched in the same figure. We observe the isotropy in Figure 3 (right).

The wave-vector k has n^2 components. As a consequence of Shanon's theorem, on a $n \times n$ frequential grid one can only consider generating surfaces with $k_s \leq \frac{n}{2L}$. Therefore, decreasing the spatial discretization parameter for a fixed size L allows representing larger wave numbers (that is to say smaller wave lengths).

Algorithm 1: Surface generator

Inputs: Φ_r, n, L ;
Give the values for the two first rows of $\mathbf{S}$ corresponding to the discretization of $[0, L]^2$;
Generate the complex random vector $\boldsymbol{\xi} = \boldsymbol{\eta} + i\boldsymbol{\zeta}$ of size n^2 , where $\boldsymbol{\eta}$ and $\boldsymbol{\zeta}$ are indep. $\mathcal{N}(\mathbf{0}, \mathbf{I})$;
Compute $\widetilde{\mathbf{\Phi}}_{\mathbf{r}}$ as the evaluation of Φ_r on the frequential grid;
Compute the elementwise product $\hat{\mathbf{q}} = \widetilde{\mathbf{\Phi}}_{\mathbf{r}}^{\frac{1}{2}} \boldsymbol{\xi}$;
Compute $\mathbf{q} = \frac{1}{n^2}$ `fftw2^-1`$(\hat{\mathbf{q}})$;
Compute the real part $\mathcal{R}(\mathbf{q})$ of $\mathbf{q}$;
Complete the third column of $\mathbf{S}$ with $\mathcal{R}(\mathbf{q})$;
Return $\mathbf{S}$;

Algorithm 1, which is a suitably modified version of the sampling method presented in [18], details the procedure to generate one realization of a rough surface on the domain $[0, L]^2$ with prescribed spectral density $\widetilde{\Phi}_r$ (that is to say for the given parameters: k_l, k_r, k_s, C, and H). The algorithm's main input is the vector $\widetilde{\mathbf{\Phi}}_{\mathbf{r}}$, which is the discrete version of $\widetilde{\Phi}_r$ and therefore contains n^2 coefficients (recall that n^2 is the number of nodes on the grid). Its output is a surface in $\mathbb{R}^3$ evaluated on the spatial grid, which is encoded as the matrix $\mathbf{S}$ of size $n^2 \times 3$ (n^2 nodes with 3 coordinates). That is, first two rows of $\mathbf{S}$ are composed of the coordinates of the nodes on the grid, while the last row is filled at the end of the algorithm with the generated surface heights.

In essence Algorithm 1 takes advantage of the fact that any affine transformation of a multivariate Gaussian random variable has a multivariate Gaussian distribution with explicitly known mean and covariance structure. The first step consists of generating the complex random vector $\boldsymbol{\xi} = \boldsymbol{\eta} + i\boldsymbol{\zeta}$, with $\boldsymbol{\eta}$ and $\boldsymbol{\zeta}$ being independent and normally distributed random vectors in $\mathbb{R}^{n^2}$ with mean zero and covariance matrix being the identity matrix of size $n^2 \times n^2$. After multiplying this vector by $\widetilde{\mathbf{\Phi}}_{\mathbf{r}}^{\frac{1}{2}}$, which is the pointwise square root of $\widetilde{\mathbf{\Phi}}_{\mathbf{r}}$, we obtain the complex vector $\hat{\mathbf{s}}$, which is then transformed to the physical space via the two-dimensional inverse Fourier transform. Finally, Algorithm 1 returns the real part of this transformation. It is noteworthy that the scaling by the factor $\frac{1}{n^2}$ in the third step of the algorithm is nec-

essary since our implementation uses the `fftw2` library [12], which has the property that $\texttt{fftw2}^{-1}(\texttt{fftw2}(\mathbf{x})) = n^2\mathbf{x}$ for any $\mathbf{x} \in \mathbb{R}^{n^2}$.

The following results guarantee that the procedure described in Algorithm 1 generates samples from a centered isotropic Gaussian field with given covariance $\widetilde{c}$ associated with the power spectral density $\widetilde{\Phi}_r$. In fact, it is a consequence of Prop. 2.9 in [24] and the fact that the power spectral density Φ_r defined in (16) has compact support.

Lemma 1. *The random surfaces generated by Algorithm 1 are mutually independent and each is a centered isotropic Gaussian field with isotropic covariance $\widetilde{c}$.*

Finally, we remark that one could also use the imaginary part of $\mathbf{q}$ as a return value for the Algorithm above so that two independent samples are generated at the same time.

3.3.1 Verification of the sampling algorithm and illustrations

The purpose of this section is to illustrate the properties of the random surface generator described in Algorithm 1. Here, we consider the parameters $k_l = 4 = k_r$, $k_s = 32$, $H = 0.8$, $L = 32$ and C is chosen so that $c(0) = 1$, which implies that the diagonal of the surface's covariance matrix Σ (i.e. the pointwise variances) is given by $\operatorname{diag}(\Sigma) = (1, 1, \ldots, 1)^T \in \mathbb{R}^{n^2}$. Moreover, we consider the grid size $h = \frac{1}{256}L$, if not specified otherwise.

First, we verify that Algorithm 1 produces samples that are centered Gaussian random fields. Specifically, we consider four trial points in the domain $D = [0, L]^2$ with coordinates $\mathbf{x}_1 = (h, h)$, $\mathbf{x}_2 = (h, h + \frac{L}{2})$, $\mathbf{x}_3 = (h + \frac{L}{2}, h)$, and $\mathbf{x}_4 = (h + \frac{L}{2}, h + \frac{L}{2})$, and approximate the distribution of each random surface point $s(\mathbf{x}_i, \omega)$, $i = 1, \ldots, 4$. To this end, we generate a sample of $N = 50000$ independent surface realizations using Algorithm 1, which is then used to approximate the probability density function (PDF) of each surface point $s(\mathbf{x}_i)$ via a kernel density estimator with Gaussian kernel and Silverman's bandwidth selection criterion; see, e.g., [19, Ch. 8.5] for details. Figure 4a shows the approximated PDFs of the surface points $s(\mathbf{x}_i, \omega)$, $i = 1, \ldots, 4$, in addition to the target $\mathcal{N}\big(0, 1\big)$ PDF. The fact that all curves are almost indistinguishable from the target PDF verifies that Algorithm 1 generates surface realizations whose surface points have the desired distribution. This conclusion is also confirmed by the Q–Q plot shown in Figure 4b. There, we plot the theoretical quantiles of the target

$\mathcal{N}(0,1)$ distribution against the quantiles obtained from the data for each surface point (color key of crosses is the same as in Figure 4a). For each of the four cases we observe an almost perfect linear trend ($y = x$), so that the data fit the target distribution very well in each case. The only regions showing minor deviations from the straight line behavior are at the very low and very high end of the range, respectively. However, these regions correspond to rare outcomes (i.e. the probability of observing values in these regions is very small), so that only a small fraction of the N samples lies in these regions, which explains the marginally worse fits in there.

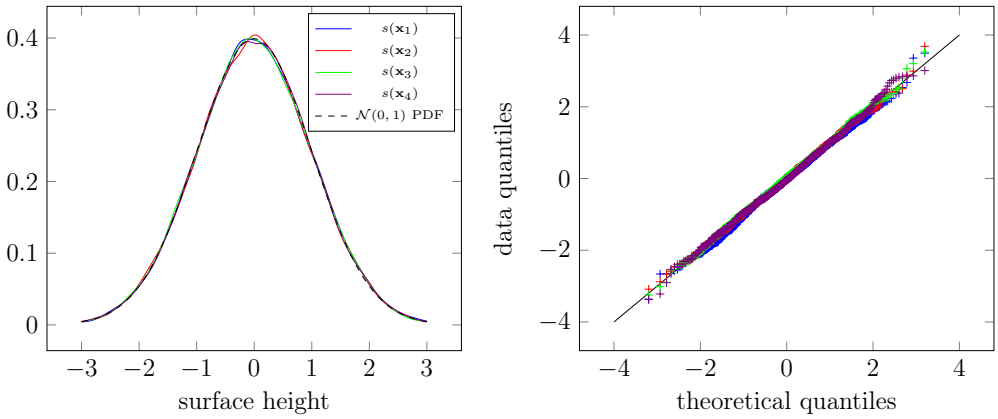

(a) PDF comparison

(b) Q–Q plot

Figure 4: Verification of surface height distribution in four points on the surface

Next, we illustrate that Algorithm 1 also produces realizations with the desired isotropic covariance. That is, we investigate the covariance matrix $\Sigma \in \mathbb{R}^{n^2 \times n^2}$ defining the n^2-dimensional Gaussian random vector obtained when evaluating Gaussian random field on the given grid. We estimate Σ via the sample covariance matrix, based on a sample of $N = 20000$ independent discrete surface realizations and we denote this estimator by $\hat{\Sigma}_N$. Inspecting the elements of $\hat{\Sigma}_N$ reveals that $\hat{\Sigma}_N$ is indeed a discretized version of an isotropic covariance. Moreover, Figure 5a shows the entries of three different estimated discretized covariance matrices as a function of r, where each matrix approximates $\mathrm{Cov}\big(s(r + L/2, L/2), s(L/2, L/2)\big)$ and is obtained for different grid sizes $h \in \{2^{-8}L, 2^{-7}L, 2^{-6}L\}$. Additionally, the plot contains the curve of the periodic target isotropic covariance $\widetilde{c}$. We observe

that Algorithm 1 generates realizations with the correct isotropic covariance structure.

Although not directly related to the quality of Algorithm 1, we also address the difference between the non-periodic isotropic covariance c and approximations to its periodic version $\widetilde{c}$. For this, Figure 5b shows two different estimated discretized covariance matrices, obtained for a fixed mesh size $h = 2^{-8}L$ but different domain sizes $L \in \{32, 64\}$, in addition to the non-periodic isotropic covariance c. We find that increasing the size L of the domain D, while keeping the grid size h fixed, leads to a more accurate approximation of the non-periodic isotropic covariance c. Indeed, with the increasing size L, the discretized spectrum tends to the continuous spectrum defined in equation (16).

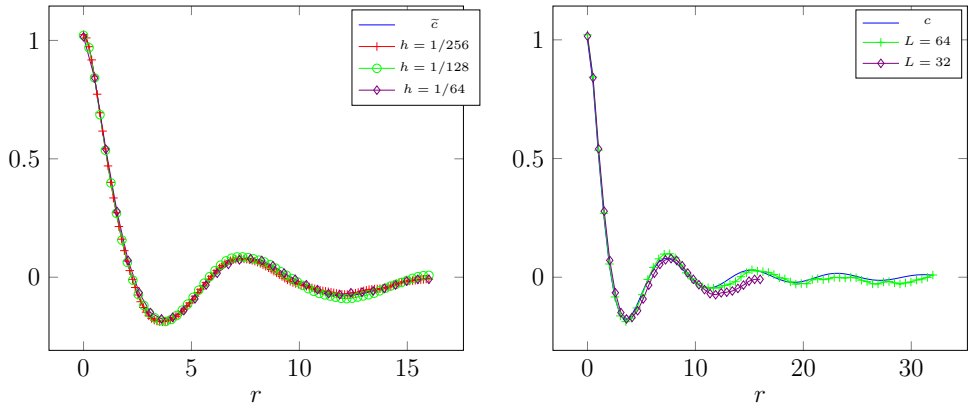

(a) Effect of the grid size h (b) Effect of the size of the domain L

Figure 5: Comparison between isotropic covariance approximations, the periodic target covariance $\widetilde{c}$, and the non-periodic version of $\widetilde{c}$.

4 Monte Carlo methods for quantifying uncertainties in rough contact mechanics

As discussed in the introduction, any quantity of interest that is derived from the solution to the contact problem is also subject to surface uncertainties. Therefore, it is crucial to understand how the surface uncertainties affect a derived quantity of interest, which in turn provides reliability measures on the numerical contact simulations. In this Section, we will describe two

Monte Carlo based sampling methods to quantify uncertainties in contact mechanics simulations. The appeal of these sampling methods is that they are non-intrusive, in the sense that an existing deterministic numerical solver does not need to be modified and can thus be considered as a black box.

Let $u = u(\omega)$ denote the solution to the continuous problem associated with the random surface $s(\omega)$, where ω denotes an elementary random event as before. The goal then is to quantify the effect of the random surface s by computing the expected value $\mathbb{E}(Q)$ of an appropriate quantity of interest Q, which is given in terms of a suitable functional F applied to the solution u, i.e. $Q(\omega) = F\big(u(\omega)\big) \in \mathbb{R}$. For example, the quantity of interest Q may be the contact area or the maximum pressure under a given load. However, as one cannot solve the continuous problem exactly, computing the expected value $\mathbb{E}(Q)$ directly based on the probability distribution of $Q(\omega)$ is unfeasible. Instead, we can only use the discretized model to obtain an approximation $Q_h(\omega) = F\big(u_h(\omega)\big)$ that converges to $Q(\omega)$ in an appropriate sense that will be specified below.

In what follows we briefly review the classic Monte Carlo method and its computational complexity for the approximation of $\mathbb{E}(Q)$ based on simulations of $Q_h(\omega)$. Afterwards we introduce the multilevel Monte Carlo method [13, 7, 34, 14] as a variant that offers drastic computational complexity improvements for a wide range of applications. See also [17] for some related earlier works. Although the focus of this work is on scalar quantities of interest, it is noteworthy that the multilevel Monte Carlo method can also be applied to multidimensional quantities as well as to parametric expectations and even for the computation of reliability measures such as quantiles and conditional values at risk [20]. We will leave the application of these options in the context of contact problems for future works.

4.1 Classic Monte Carlo method

The classic Monte Carlo (MC) estimator is defined as the mean of a sample of N independent and identically distributed (i.i.d.) realizations of Q_h, that is

$$E^{\mathrm{MC}}(Q_h) := \frac{1}{N} \sum_{j=1}^{N} Q_h\big(\omega^{(j)}\big) \,, \tag{18}$$

where $Q_h\big(\omega^{(j)}\big)$, $j = 1, ..., N$, is a sequence of independent and identically distributed variables, all distributed as $Q_h(\omega)$. The accuracy of the Monte

Carlo estimator $E_N^{\mathrm{MC}}(Q_h)$ as an approximation of $\mathbb{E}(Q)$ can be characterized via the mean squared error, viz.

$$\mathbb{E}\Big(\big(\mathbb{E}(Q) - E_N^{\mathrm{MC}}(Q_h)\big)^2\Big) = \frac{\mathrm{Var}(Q_h)}{N} + \mathbb{E}(Q - Q_h)^2 \,. \tag{19}$$

Here, the first term on the right-hand side (the so-called statistical error) quantifies the estimator's variance and is inversely proportional to the number of realizations N. The second term (the so-called squared bias) accounts for the expected error due to discretization errors and depends on the numerical method used to generate the realizations. Clearly, for E_N^{MC} to be an efficient approximation of $\mathbb{E}(Q)$ both terms should be balanced. To further characterize the computational complexity of the Monte Carlo method, it is reasonable to consider a numerical method for which the bias vanishes while the computational cost increases as $h \to 0$. Specifically, we will assume that

MC-1 the cost to compute each i.i.d. realization of Q_h is bounded by $\mathrm{cost}(Q_h) \leq C_\gamma h^{-\gamma}$ for some constants $C_\gamma, \gamma > 0$,

MC-2 the bias decays with order $\alpha > 0$, in the sense that $|\mathbb{E}(Q - Q_h)| \leq C_\alpha h^\alpha$ for some constant $C_\alpha > 0$,

MC-3 the variance of Q_h is uniformly bounded in h for $h \ll 1$.

These assumptions are in fact adequate for the contact problems considered here. For example, Assumption **MC-2** is related to properties of the boundary element method for each deterministic problem; cf. [6]. Similarly, we expect that the cost of the iterative scheme used to approximate the solution to the contact problem is proportional to a power law with respect to the grid size h, since the grid size controls both the accuracy and the dimension of the discretized problem.

When balancing the bias and the statistical error to achieve a mean squared error of order ε^2 in (19), it is thus sufficient to choose[1]

$$h \simeq \varepsilon^{1/\alpha} \quad \text{and} \quad N \simeq \varepsilon^{-2} \,. \tag{20}$$

Consequently, the corresponding total work that is required for the MC estimator to achieve an order ε^2 mean squared error tolerance is given by

$$\mathrm{W}\big(E_N^{\mathrm{MC}}(Q_h)\big) = N\mathrm{cost}(Q_h) \lesssim \varepsilon^{-2-\frac{\gamma}{\alpha}} \,. \tag{21}$$

[1]We use the notation $a \lesssim b$, if there exists a constant c>0, such that $a \leq cb$; analogously for $\gtrsim$. If $a \lesssim b$ and $a \gtrsim b$, then we write $a \simeq b$.

4.2 Multilevel Monte Carlo method

The underlying idea of the multilevel Monte Carlo (MLMC) method is to use realizations of approximations to Q with varying accuracy. Specifically, we consider a hierarchy of M grids, called levels, with grid sizes $h_0 > h_1 > \cdots > h_M$. As we will see below, the grid size h_M of the finest discretization level takes over the role of the grid size used in the classic MC method above. We denote by Q_{h_ℓ} the approximation of Q on level ℓ, that is $Q_{h_\ell} = F(u_{h_\ell})$ where u_{h_ℓ} solves the discretized problem on a grid with size h_ℓ. Using the linearity of the expectation operator, one can then write the expectation of the approximation of Q on the finest level h_M as a telescoping sum. That is, $\mathbb{E}\big(Q_{h_M}\big)$ can be written as the expectation of the approximation of Q on the coarsest level h_0 plus a sum of correction terms that are expectations of approximations on consecutive levels:

$$\mathbb{E}\big(Q_{h_M}\big) = \mathbb{E}\big(Q_{h_0}\big) + \sum_{\ell=1}^{M} \mathbb{E}\big(Q_{h_\ell} - Q_{h_{\ell-1}}\big) \equiv \sum_{\ell=0}^{M} \mathbb{E}\big(\Delta_\ell\big) \,, \tag{22}$$

where $\Delta_0 := Q_{h_0}$ and $\Delta_\ell := Q_{h_\ell} - Q_{h_{\ell-1}}$ for $\ell > 0$. The MLMC estimator $E^{\mathrm{MLMC}}(Q_{h_M})$ is then obtained by approximating each of the expectations $\mathbb{E}(\Delta_\ell)$ by a MC estimator using N_ℓ i.i.d. realizations:

$$\begin{aligned} E^{\mathrm{MLMC}}(Q_{h_M}) &:= \sum_{\ell=0}^{M} \frac{1}{N_\ell} \sum_{j=1}^{N_\ell} \Delta_\ell\big(\omega_\ell^{(j)}\big) \\ &= \frac{1}{N_0} \sum_{j=1}^{N_0} Q_{h_0}\big(\omega_0^{(j)}\big) + \sum_{\ell=1}^{M} \frac{1}{N_\ell} \sum_{j=1}^{N_\ell} \Big(Q_{h_\ell}\big(\omega_\ell^{(j)}\big) - Q_{h_{\ell-1}}\big(\omega_\ell^{(j)}\big) \Big) \,. \end{aligned} \tag{23}$$

Notice that the correction terms $\Delta_\ell := Q_{h_\ell} - Q_{h_{\ell-1}}$ are computed using the same random realization on both levels ℓ and $\ell - 1$, while the Δ_ℓ terms are sampled independently on different levels.

As for the MC estimator, the accuracy of the MLMC estimator is commonly assessed via the mean squared error, which can also be decomposed into the statistical error and the squared bias:

$$\mathbb{E}\Big(\big(\mathbb{E}(Q) - E^{\mathrm{MLMC}}(Q_{h_M}) \big)^2 \Big) = \sum_{\ell=0}^{M} \frac{\mathrm{Var}\big(\Delta_\ell\big)}{N_\ell} + \mathbb{E}(Q - Q_{h_M})^2 \,. \tag{24}$$

The identity above demonstrates the virtue of considering multiple levels instead of just one fine grid. In fact, if $\mathrm{Var}\big(\Delta_\ell\big)$ decreases as ℓ increases, then one may need many realizations only on the coarse levels, which are typically cheap to generate, but only very few on the finer, more expensive, levels. To make this intuition precise, we will assume that

ML-1 the cost to compute each i.i.d. realization of Q_{h_ℓ} is bounded by $\mathrm{cost}(Q_{h_\ell}) \leq C_\gamma {h_\ell}^{-\gamma}$ for all $\ell >$ and some constants $C_\gamma, \gamma > 0$,

ML-2 the bias decays with order $\alpha > 0$, in the sense that $|\mathbb{E}(Q - Q_{h_\ell})| \leq C_\alpha {h_\ell}^{\alpha}$ for all $\ell >$ and some constant $C_\alpha > 0$,

ML-3 the variance of $\Delta_\ell = Q_{h_\ell} - Q_{h_{\ell-1}}$ decays with rate $\beta > 0$, in the sense that $\mathrm{Var}\big(\Delta_\ell\big) \leq C_\beta {h_\ell}^{\beta}$ for all $\ell >$ and some constant $C_\beta > 0$.

Notice that assumptions **ML-1** and **ML-2** for the MLMC method are the same as assumptions **MC-1** and **MC-2** for the MC method.

In this work we will consider geometric grids, in the sense that $h_\ell = \delta^{-\ell} h_0$ for some $\delta > 1$. In practice the value $\delta = 2$ is often used, which we also adopt here. Although a non-optimal choice of δ can affect the MLMC method's performance [16], this effect is minor. Under the assumptions above with $2\alpha \geq \min(\beta, \gamma)$, it can then be shown (see [14]), that for any $e^{-1} > \varepsilon > 0$ there exist parameters M and $\big(N_\ell\big)_{\ell=0,\ldots,M}$ such that the corresponding MLMC estimator achieves an order ε^2 mean squared error tolerance with total computational work bounded by

$$\mathrm{W}\big(E_N^{\mathrm{MLMC}}(Q_{h_M})\big) = \sum_{\ell=0}^{M} N_\ell \,\mathrm{cost}(\Delta_\ell) \lesssim \begin{cases} \varepsilon^{-2}\,, & \beta > \gamma\,, \\ \varepsilon^{-2}\log(\varepsilon)^2\,, & \beta = \gamma\,, \\ \varepsilon^{-2-\frac{\gamma-\beta}{\alpha}}\,, & \beta < \gamma\,. \end{cases} \tag{25}$$

The complexity result above follows from solving a constrained optimization problem, which also reveals the necessary parameter choices

$$h_M \simeq \varepsilon^{1/\alpha} \Rightarrow M \simeq \frac{\log_\delta\big(\varepsilon^{-1}\big)}{\alpha} \quad \text{and} \quad N_l \simeq \varepsilon^{-2}\sqrt{\frac{\mathrm{Var}\big(\Delta_l\big)}{\mathrm{cost}(\Delta_l)}}\sum_{\ell=0}^{M}\sqrt{\mathrm{Var}\big(\Delta_\ell\big)\,\mathrm{cost}(\Delta_\ell)}\,, \tag{26}$$

for $l = 0, \ldots, M$. The complexity bound in (25) also depicts the importance of the parameter β that controls the variance decay of the differences Δ_ℓ; see assumption **ML-3**. Moreover, comparing the complexity results (21)

and (25), we find that the computational work for $\beta > \gamma$ is primarily on the coarsest levels, in the sense that the overall complexity of the MLMC method is dominated by the MC method on the coarse level and the additional work on finer levels is negligible in that case. Conversely, for $\beta < \gamma$ the main work contribution originates form the finest level. For the borderline case $\beta = \gamma$ the work is spread across all levels. It is noteworthy that even in the worst case (i.e. when $\beta < \gamma$) the MLMC still provides complexity improvement of order $\varepsilon^{\beta/\alpha}$ over the MC method.

4.2.1 Comments on the application to random contact mechanics

For the practical application of the MLMC method to the contact problem at hand, a few comments are in order. Firstly, the coarsest grid size h_0 should be chosen sufficiently small so that a basic problem resolution is provided and also such that $\frac{L}{h_0}$ is an integer. That is, the coarsest grid size is related to the roughness of the surface since we aim at accurately representing the largest wavelengths of size L/k_l. A heuristics would be to chose $h_0 = 10\frac{L}{k_l}$ in order to resolve the largest asperity. Secondly, assembling the MLMC estimator (23) requires to compute realizations of the differences $\Delta_\ell = Q_{h_\ell} - Q_{h_{\ell-1}}$ on the different levels. Specifically, one has to compute these differences of approximations on consecutive grids for the same random event ω_ℓ, i.e. for the same realization of the random surface $s(\omega_\ell)$ on both level ℓ and level $\ell - 1$. This can, for example, be done by generating a realization of the discretized surface associated with the grid on level ℓ using Algorithm 1, which is then used to compute the corresponding realization of Q_{h_ℓ}. The version of the surface on level $\ell - 1$, required to compute $Q_{h_{\ell-1}}$, is then obtained by projecting the realization of discretized surface on level ℓ onto the coarser (nested) grid of level $\ell - 1$. This particular approach offers the additional advantage that one can use the solution to the contact problem on level ℓ, after projecting it on the grid on level $\ell - 1$, as initial condition for the iterative solver for the contact problem on the coarser level; see Sect. 2. Indeed, this procedure can significantly reduce the computational effort for solving the problem on the coarser level $\ell - 1$.

5 Numerical Experiments

In this section, we consider two different quantities of interest that are derived from the solution to the contact problem. The first one is the total contact area under a given load $\bar{p}$. This is a global quantity, which is straightforward to estimate once the contact problem is solved, and it is of major interest in many engineering applications. For instance, the thermal conductivity between solids is proportional to the contact area. The second quantity is the number of contact clusters under load $\bar{p}$. This quantity describes the morphology of the contact area and it is of interest, for example, in leakage problems.

The numerical experiments that follow were carried out in Python on a standard laptop computer with 7.7 GB of memory and an Intel®Core™ i7-5600U processor. Moreover, for the contact problems, we consider the wave numbers $k_l = 1$, $k_r = 1$, $k_s = 64$, $H = 0.8$, and C is chosen such that $c(0) = 1$. Notice that the ratio $\lambda_l/\lambda_s = k_s/k_l$ is large to model a surface's self-affinity across a wide range of frequencies. We also note that the Hurst exponent $H = 0.8$ is motivated by the experimental results published in [25]. Furthermore, Young's modulus E and the Poisson ratio ν are such that the equivalent modulus is $E^\star = \frac{E}{1-\nu^2} = 1$.

5.1 The real contact area

To study the effects of the surface uncertainties to the real contact area, we consider the random quantity of interest Q given as the normalized contact area (in percent):

$$Q(\omega) = \frac{100}{|D|} \int_D \mathbb{I}_{g(\mathbf{x},\omega)=0} \, d\mathbf{x} \, . \tag{27}$$

For this quantity of interest, we set the applied load to be $\bar{p} = \frac{0.1}{\sqrt{m_2}}$, where m_2 is the second spectral moment of the rough surface s so that $\sqrt{m_2}$ is the root mean square of the slopes (see [38] for its computation).

In the discretized problem, since we obtain piecewise constant solutions, the contact area is therefore computed as

$$Q_h(\omega) = \frac{1}{n^2} \sum_{i \in I_c(\omega)} 1 \, , \tag{28}$$

where the set of contact points I_c is defined by: $i \in I_c(\omega) \Leftrightarrow u_i(\omega) - s_i(\omega) = 0$.

	Box size L			
	1	2	3	4
$E^{\mathrm{MC}}(Q_L)$	19.52	19.90	19.94	19.99

Table 1: MC estimators of the contact area for various box sizes L.

5.1.1 Choosing the surface size L

What is not considered yet is the error introduced by the domain truncation and the PBCs, which is generally difficult to assess since the continuous solutions of problems $\mathcal{P}^L$ and $\mathcal{P}$ are not accessible. To nonetheless identify the size L of the truncated problem such that model error $\mathcal{P}-\mathcal{P}^L$ does not dominate the overall error in the the numerical study that follows, we numerically investigate this effect. Specifically, we estimate the expectation of the contact area Q_L via $E^{\mathrm{MC}}(Q_L)$ for different domain truncations $L \in \{1,2,3,4\}$. For each size L, we compute 50 i.i.d realizations, where the discretization parameter h is chosen such that the discretization error is negligible. Indeed, we choose $h = 1/512$ in order to properly describe the smallest wavelength λ_s (8 nodes per wavelength). Of course, by changing the size of the surface, the number of grid points increases but h remains constant. The obtained results are summarized in the Table 1. We observe that $E^{\mathrm{MC}}(Q_L)$ seems to monotonically approach the limit value $\bar{Q}_\infty = 20$ as L increases. In fact, the distance to the limit value is $|E^{\mathrm{MC}}(Q_L) - \bar{Q}_\infty| \leq 0.1$ for $L \geq 2$. Notice that an absolute error of 0.1 already corresponds to a relative error of 0.5%. Therefore, we decided to choose $L = 2$ for the numerical study that follows, for which we will then explore mean squared error tolerances ε^2 for $0.2 \leq \varepsilon$. Consequently, we can be confident that the model error is not dominating the overall error, in the sense that it is at most comparable to the prescribed mean squared error tolerance. Finally, we note that the numerical investigation of the model error carried out here was somewhat ad-hoc. A more systematic treatment seems possible by means of the so-called multi-index Monte Carlo method [15], which allows to construct a hierarchy with respect to both the h discretization and the domain truncation L. This more complex analysis is work in progress (see also Sect. 6) and will be presented elsewhere.

5.1.2 Verifying the Assumptions for the MLMC

Before we use the MLMC method described in Sect. 4 to estimate the expectation of Q, we verify that the Assumptions **ML-1**–**ML-3** are satisfied. We reiterate that assumptions **ML-1** and **ML-2** coincide with assumptions **MC-1** and **MC-2** for the classic Monte Carlo method, so that their validity is also essential to optimally tune the Monte Carlo method. To the authors' knowledge, no theoretical convergence results concerning these hypotheses for the contact problem solved with the discretization method used in this paper are available. We thus estimate the characterizing rates using the techniques described in [14], which is based on an initial screening phase where the rates are estimated via linear regression. Here, this screening phase was carried out for various grid sizes $h_\ell = h_0 2^{-\ell}$, using 50 realizations for each resolution, which was sufficient here. The coarsest grid considered was 128×128. Figures 6 and 7 show the outcomes of this screening procedure.

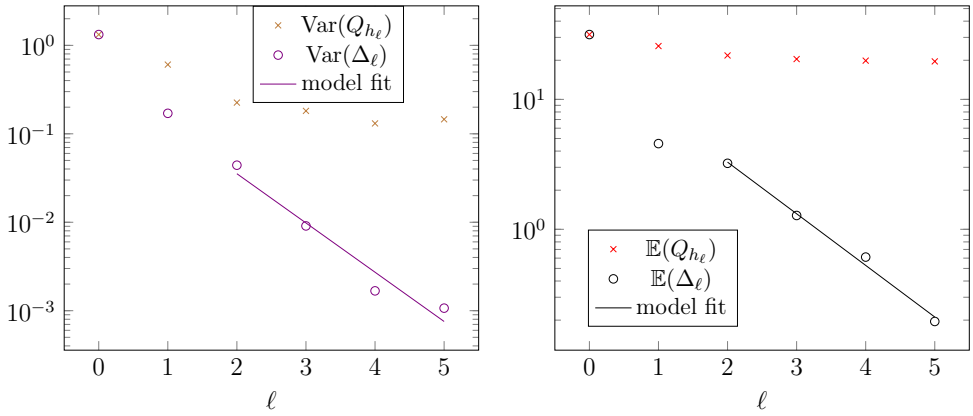

(a) Variance decay

(b) Bias decay

Figure 6: Estimation of convergence rates.

We find that this screening procedure yields $\alpha = 1.32$, $C_\alpha = 20.5$, $\beta = 1.85$, $C_\beta = 0.46$, $\gamma = 2.45$, and $C_\gamma = 1.69$. It is noteworthy that the coefficient γ only depends on the implementation of the contact solver, but not on the machine used for the simulations; the machine dependence only affects the constant C_γ. The obtained rates β and γ thus indicate that a MLMC method will provide a computational complexity of order $\mathcal{O}(\varepsilon^{-2-\frac{\gamma-\beta}{\alpha}}) = \mathcal{O}(\varepsilon^{-2.26})$, in contrast to a classic MC method with computational complexity of order $\mathcal{O}(\varepsilon^{-2-\frac{\gamma}{\alpha}}) = \mathcal{O}(\varepsilon^{-3.66})$.

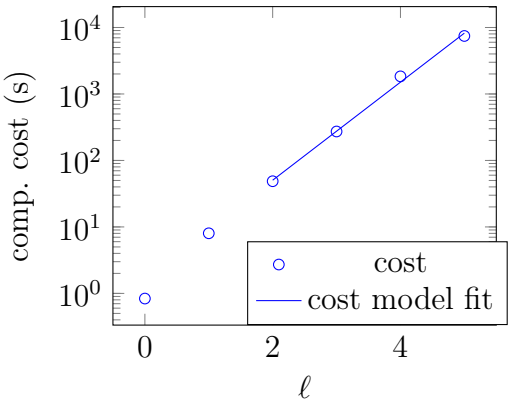

Figure 7: Estimation of the cost model.

	tolerance ε								
	1.0	0.9	0.8	0.7	0.6	0.5	0.4	0.3	0.2
$E^{\mathrm{MC}}(Q_h)$	19.94	20.26	19.90	20.11	19.48	19.55	19.64	19.97	20.01
$E^{\mathrm{MLMC}}(Q_h)$	19.42	19.57	19.53	19.53	19.74	19.59	19.65	20.09	20.03
ε_r (%)	5 %	4.5 %	4 %	3.5 %	3 %	2.5 %	2 %	1.5 %	1 %

Table 2: MC and MLMC estimators of the contact area for various tolerances.

5.1.3 Estimation of the real contact area

Motivated by the screening process for the rates (see Fig. 6), we set the coarsest level of the MLMC grid hierarchy to be a 256×256 grid. Based on the coarsest level grid size h_0 and the estimated rates, we can thus use the formulas in (26) to construct the MLMC estimator to approximate the mean real contact area for a given tolerance. Table 2 shows the estimated expectation of the true contact area computed via both the classic Monte Carlo method $E^{\mathrm{MC}}(Q_h)$ and the multilevel Monte Carlo method $E^{\mathrm{MLMC}}(Q_h)$ for different tolerances ε. As the exact value of $\mathbb{E}(Q)$ is not known, we cannot exactly assess the approximation error. However, it can be seen in Table 2 that both estimators provide similar results. In fact, the estimated values always satisfy

$$|E^{\mathrm{MC}}(Q_h) - E^{\mathrm{MLMC}}(Q_h)| \leq 2\varepsilon \,, \tag{29}$$

	tolerance ε								
	1.0	0.9	0.8	0.7	0.6	0.5	0.4	0.3	0.2
W_{MC} (s)	37	37	41	220	243	374	531	2090	5019
W_{MLMC} (s)	36	37	38	142	176	200	226	500	629
$\frac{W_{\mathrm{MC}}}{W_{\mathrm{MLMC}}}$	0.97	1	1.1	1.55	1.38	1.87	2.34	4.18	7.97

Table 3: Cost (in seconds) to compute the MC and MLMC estimators of the contact area for various tolerances.

which confirms the theoretical mean squared error results discussed in Sect. 4. It is noteworthy that the mean squared error criterion is an absolute error criterion. To ease the interpretation of the used tolerance ε, we have also added the relative precision $\varepsilon_r = \frac{\varepsilon}{E^{\mathrm{MLMC}}(Q_h)}$ to the table. Furthermore, we report that both the MC estimator's and the MLMC estimator's variance is of order $\mathcal{O}(\varepsilon^2)$ for all experiments as required. These variance estimates can, for example, be obtained from formulas (19) and (24), respectively, using the results of the screening phase (see Sect. 5.1.2), or via an additional Monte Carlo estimation. For large values of ε the estimation via MC or MLMC gives better results than required. This could be explained by the fact that the number of levels as well as the numbers of samples per level have to be integers. This is achieved by applying the ceiling function to the formulas in (26). Consequently, the simulation outcomes may be overly conservative with respect to the required tolerance. In fact, this effect may be more pronounced for larger tolerances than for smaller ones.

While Table 2 compares the estimated mean contact area for various values of the tolerance ε, Table 3 summarizes the corresponding computational times required to obtain said estimators. Specifically, in Table 3, we present the computational time in seconds for the classic Monte Carlo method (denoted by W_{MC}) and for the multilevel Monte Carlo method (W_{MLMC}) for different prescribed tolerance requirements. These results confirm the performance gains described in Sect. 4 and clearly demonstrates that the multilevel Monte Carlo method is highly efficient. Indeed, the smaller the tolerance ε, the more drastic the gain. The data presented in Table 3 are also illustrated in Figure 8 in addition to the theoretical complexity results (i.e. Eq. (21) and Eq. (25)). The plot shows that the measured computational times are in good agreement with theoretical complexity results. The discrepancy obtained for

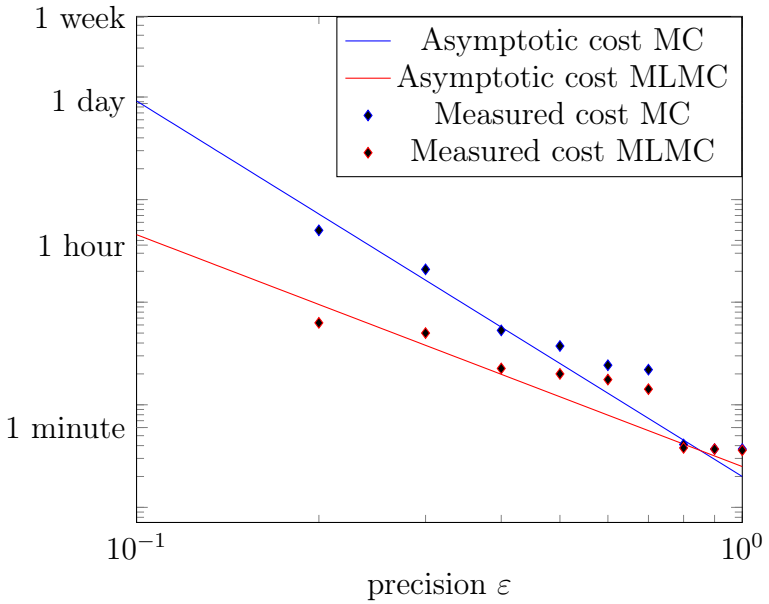

Figure 8: Theoretical and measured costs for the MC and the MLMC estimators for different tolerances. The quantity of interest is the contact area.

relatively large tolerance values ε can be explained by the small amount of time required to compute the estimation so that the cost is dominated by post-processing steps.

Figure 9 moreover presents the number of realizations required for two different prescribed tolerances for both the MC method and the MLMC method. For the tolerance $\varepsilon = 0.7$, Table 3 shows that the cost of the MC method is only marginally higher than the cost of MLMC method, while Figure 9a indicates that the distribution of required realizations (i.e. the work) across levels is very different. This is even more so for a tolerance of $\varepsilon = 0.2$, as can be seen in Figure 9b. In fact, the MLMC method spreads the number of realizations across various levels with requiring most realizations on the coarse (cheap) grids and only few on the finer (more expensive) grids, whereas the MC requires all of the many realizations on the finest grid (most expensive).

5.2 The number of contact clusters

The second quantity of interest we study here is the number of contact clusters (i.e. the number of contact zones) per square meters under the given load

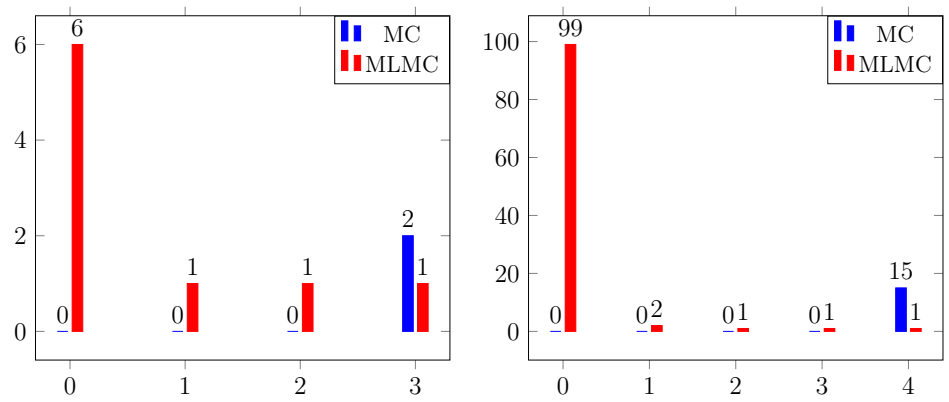

(a) $\varepsilon = 0.7$ (b) $\varepsilon = 0.2$

Figure 9: Number of realizations required per level for both the Monte Carlo method and the multilevel Monte Carlo method for two tolerances.

Figure 10: Binary contact map: contact zones are in black.

$\bar{p} = \frac{0.1}{\sqrt{m_2}}$. That is, we consider the random quantity of interest $\frac{Q}{L^2}$, which is such that

$$\big\{\mathbf{x} \in D\colon g(\mathbf{x}, \omega) = 0\big\} = \bigcup_{q=1}^{Q(\omega)} \mathcal{Z}_q(\omega) \tag{30}$$

where $\mathcal{Z}_q(\omega)$ are the individual, disjoint contact zones. Mathematically, Q is the number of connected components of the set $\{\mathbf{x} \in D\colon g(\mathbf{x}) = 0\}$. Interested reader may refer to [11] for the computation of connected components of graphs. An illustration is given in Figure 10 that exhibits 11 contact clusters.

	Box size L			
	1	2	3	4
$E^{\mathrm{MC}}(Q_L)$	93.1	104.1	110.2	109.4

Table 4: MC estimators of the mean number of contact clusters for various box sizes L.

5.2.1 Choosing the surface size L

To identify the size L of the truncated problem such that model error $\mathcal{P}-\mathcal{P}^L$ does not dominate the overall error in the the numerical study that follows, we proceed exactly as for the first quantity of interest. The corresponding results are summarized in the Table 4. There, we see that $E^{\mathrm{MC}}(Q_L)$ seems to approach the limit value $\bar{Q}_\infty = 110$ as L increases. More precisely, the distance to the limit value is $|E^{\mathrm{MC}}(Q_L) - \bar{Q}_\infty| \leq 1$ for $L \geq 3$. Note that an absolute error of 1 already corresponds to a relative error smaller than 1%. As a consequence, we decided to choose $L = 3$ for the numerical study that follows, for which we will then explore mean squared error tolerances ε^2 for $2 \leq \varepsilon$. Having to choose a different box size L than for the first quantity of interest is not surprising since mechanical quantities are not affected the same way by the PBCs.

5.2.2 Estimation of convergence rates

We estimate the rates needed for the MLMC method using the same screening procedure as for the first quantity of interest. This procedure yields $\alpha = 2.79$, $C_\alpha = 211$, $\beta = 2.41$, $C_\beta = 42.6$, $\gamma = 2.53$, and $C_\gamma = 318$. Overall, the MLMC method will provide a computational complexity of order $\mathcal{O}(\varepsilon^{-2-\frac{\gamma-\beta}{\alpha}}) = \mathcal{O}(\varepsilon^{-2.04})$ here, while the MC method will yield a computational complexity of order $\mathcal{O}(\varepsilon^{-2-\frac{\gamma}{\alpha}}) = \mathcal{O}(\varepsilon^{-2.90})$.

5.2.3 Estimation of the number of contact clusters

Guided by the screening procedure, we set the coarsest level to be a 128×128 grid and use both the MC method and MLMC method to approximate the mean number of contact clusters for various required tolerances $\varepsilon \in \{40, 30, 20, 15, 10, 9, 8, 7, 6, 5, 4, 3, 2\}$.

	tolerance ε											
	40	30	20	15	10	9	8	7	6	5	4	
$E^{\mathrm{MC}}(Q_h)$	105.1	109.8	123.7	105.1	110.1	108.3	102.7	108.5	109.8	112.6	109.4	10
$E^{\mathrm{MLMC}}(Q_h)$	108.8	102.2	112.5	108.9	115.4	108.4	111.1	107.9	110.8	113.5	111.3	11
ε_r (%)	37 %	29 %	17 %	14 %	8.6 %	8.3 %	7.2 %	6.5 %	5.4 %	4.4 %	3.6 %	2.

Table 5: Estimations of the mean number of contact clusters for different tolerances with the MC method and the MLMC method.

In Table 5, we then present the approximations $E^{\mathrm{MC}}(Q_h)$ and $E^{\mathrm{MLMC}}(Q_h)$, respectively, of the expected number of contact clusters $\mathbb{E}(Q)$ computed with the MC method and the MLMC method, respectively, for the tolerances introduced above. As in the previous example, the exact value of $\mathbb{E}(Q)$ is not known. However, the results in Table 5 show that

$$|E^{\mathrm{MC}}(Q_h) - E^{\mathrm{MLMC}}(Q_h)| \leq 2\varepsilon \,, \tag{31}$$

thus verifying the tolerance requirement. We also add in the same table the relative precision $\varepsilon_r = \frac{\varepsilon}{E^{\mathrm{MLMC}}(Q_h)}$ for an easier interpretation. The results in Table 5 also reveal that both MC and MLMC estimators seem to overkill the desired tolerance. A possible explanation for this phenomenon is that the coarsest grid may not allow to accurately represent small wavelengths, which thus leads to a smaller variance in the number of contact clusters.

Finally, in Table 6 we report the computational time in seconds for both the Monte Carlo method (W_{MC}) and multilevel Monte Carlo method (W_{MLMC}), each for different tolerance requirements ε. Once again we observe that the MLMC method is not only highly competitive, but actually superior for any tolerance demand larger than 15. Indeed, the smaller ε, the larger the gain.

6 Conclusion

In this work, we have applied the multilevel Monte Carlo method to estimate quantities of interest related to the problem of frictionless normal contact of rough surfaces. After describing the statistical properties of the random rough surfaces in detail, we first verified that a variant of the surface generator introduced in [18] generates samples of rough surfaces with

	tolerance ε												
	40	30	20	15	10	9	8	7	6	5	4	3	2
W_{MC} (s)	90	90	96	170	262	407	420	649	2209	4752	4782	18806	18735
W_{MLMC} (s)	107	107	107	118	118	123	125	129	477	507	523	836	848
$\frac{W_{\mathrm{MC}}}{W_{\mathrm{MLMC}}}$	0.84	0.84	0.89	1.44	2.22	3.3	3.36	5.03	4.63	9.37	9.14	22.49	22.09

Table 6: Cost (in seconds) required to compute the estimation of the mean number of contact clusters for different tolerances with the MC method and the MLMC method.

the desired statistical properties. Then, we briefly reviewed the principles of the multilevel Monte Carlo method as an efficient sampling based technique to quantify uncertainties in random system outputs. Afterwards, we detailed how to use the MLMC method effectively in the context of rough contact problem and demonstrated by means of numerical assessments the huge computational gain that the MLMC methods provides compared to the classic Monte Carlo method.

Future work building upon the framework presented here, consists, for example, of studying other quantities of interest, such as the percentage of the surface subject to a pressure larger than a given critical pressure or even functional quantities such as the pressure field itself. Another interesting direction is to estimate higher order moments of a quantity of interest, such as the variance. This will be especially interesting in the context of quantifying distributions of the quantity when considering the error due to the size L of the simulation box in addition to the discretization error. Consequently, future work will go in that direction, by taking advantage of the so-called multi-index Monte Carlo method [15].

Acknowledgments

Support for V.R. from the 'EPFL Fellows' fellowship program co-funded by Marie Skłodowska-Curie, Horizon 2020 Grant agreement no. 665667 is gratefully acknowledged. The authors would like to thank Professor Jean-François Molinari and Guillaume Anciaux for helpful discussions.

References

[1] M. Abramowitz and I. A. Stegun. *Handbook of mathematical functions with formulas, graphs, and mathematical tables*. Dover, 1964.

[2] Alberto Bemporad and Marco Paggi. Optimization algorithms for the solution of the frictionless normal contact between rough surfaces. *International Journal of Solids and Structures*, 69:94–105, 2015.

[3] C. Bierig and A. Chernov. Approximation of probability density functions by the multilevel Monte Carlo maximum entropy method. *J. Comput. Phys.*, 314:661–681, 2016.

[4] C. Bierig and A. Chernov. Estimation of arbitrary order central statistical moments by the multilevel Monte Carlo method. *Stoch. Partial Differ. Equ. Anal. Comput.*, 4(1):3–40, 2016.

[5] Claudio Bierig and Alexey Chernov. Convergence analysis of multilevel monte carlo variance estimators and application for random obstacle problems. *Numerische Mathematik*, 130(4):579–613, 2015.

[6] Carlos Alberto Brebbia, José Claudio Faria Telles, and Luiz Wrobel. *Boundary element techniques: theory and applications in engineering*. Springer Science and Business Media, 2012.

[7] K. A. Cliffe, M. B. Giles, R. Scheichl, and A. L. Teckentrup. Multilevel monte carlo methods and applications to elliptic PDEs with random coefficients. *Computing and Visualization in Science*, 14(1):3, 2011.

[8] A. Corigliano, R. Ardito, C. Comi, A. Frangi, A. Ghisi, and S. Mariani. Microsystems and mechanics. *Procedia IUTAM*, 10:138–160, 2014.

[9] HL Costa and IM Hutchings. Hydrodynamic lubrication of textured steel surfaces under reciprocating sliding conditions. *Tribology International*, 40(8):1227–1238, 2007.

[10] Yalchin Efendiev, Cornelia Kronsbein, and Frédéric Legoll. Multilevel monte carlo approaches for numerical homogenization. *Multiscale Modeling & Simulation*, 13(4):1107–1135, 2015.

[11] Pedro F Felzenszwalb and Daniel P Huttenlocher. Efficient graph-based image segmentation. *International journal of computer vision*, 59(2):167–181, 2004.

[12] M. Frigo and S.G. Johnson. The design and implementation of FFTW3. *Proceedings of the IEEE*, 93(2):216–231, 2005.

[13] M. B. Giles. Multilevel Monte Carlo path simulation. *Oper. Res.*, 56(3):607–617, 2008.

[14] M. B. Giles. Multilevel monte carlo methods. *Acta Numerica*, 24:259, 2015.

[15] A.-L. Haji-Ali, F. Nobile, and R. Tempone. Multi-index Monte Carlo: when sparsity meets sampling. *Numer. Math.*, 132(4):767–806, 2016.

[16] A.-L. Haji-Ali, F. Nobile, E. von Schwerin, and R. Tempone. Optimization of mesh hierarchies in multilevel Monte Carlo samplers. *Stoch. Partial Differ. Equ. Anal. Comput.*, 4(1):76–112, 2016.

[17] S. Heinrich. Multilevel Monte Carlo methods. In *Large-Scale Scientific Computing*, pages 58–67. Springer, 2001.

[18] Y. Z. Hu and K. Tonder. Simulation of 3-D random rough surface by 2-D digital filter and fourier analysis. *International Journal of Machine Tools and Manufacture*, 32:83–90, 1992.

[19] D. P. Kroese, T. Taimre, and Z. I. Botev. *Handbook of Monte Carlo Methods*. John Wiley and Sons, 2011.

[20] S. Krumscheid and F. Nobile. Multilevel Monte Carlo approximation of functions. submitted. Available as Mathicse Report no. 12.2017, 2017.

[21] G. J. Lord, C. E. Powell, and T. Shardlow. *An Introduction to Computational Stochastic PDEs*. Cambridge University Press, New York, 2014.

[22] B Lorenz, BNJ Persson, G Fortunato, M Giustiniano, and F Baldoni. Rubber friction for tire tread compound on road surfaces. *Journal of Physics: Condensed Matter*, 25(9):095007, 2013.

[23] P. Ranganath Nayak. Random process model for rough surfaces. *Journal of lubrication Technology*, 108(3):398–407, 1971.

[24] F. Nobile. *Numerical Approximation of random PDEs*. Lecture notes, EPFL, 2016.

[25] B. N. J. Persson, O. Albohr, U. Tartaglino, A. I. Volokitin, and E. Tosatti. On the nature of surface roughness with application to contact mechanics, sealing, rubber friction and adhesion. *Journal of Physics: Condensed Matter*, 17(1):R1, 2005.

[26] M. Pisaroni, F. Nobile, and P. Leyland. A Continuation Multi Level Monte Carlo (C-MLMC) method for uncertainty quantification in compressible inviscid aerodynamics. *Comput. Methods Appl. Mech. Engrg.*, 326:20–50, 2017.

[27] R. Pohrt and V. L. Popov. Normal contact stiffness of elastic solids with fractal rough surfaces. *Physical Review Letters*, 93:104301+, 2012.

[28] I. A. Polonsky and L. M. Keer. A numerical method for solving rough contact problems based on the multi-level multi-summation and conjugate gradient techniques. *Wear*, 231(2):206 – 219, 1999.

[29] Nikolay Prodanov, Wolf B Dapp, and Martin H Müser. On the contact area and mean gap of rough, elastic contacts: Dimensional analysis, numerical corrections, and reference data. *Tribology Letters*, 53(2):433–448, 2014.

[30] C Putignano, L Afferrante, G Carbone, and G Demelio. The influence of the statistical properties of self-affine surfaces in elastic contacts: A numerical investigation. *Journal of the Mechanics and Physics of Solids*, 60(5):973–982, 2012.

[31] C. Putignano, L. Afferrante, G. Carbone, and G. Demelio. A new efficient numerical method for contact mechanics of rough surfaces. *International Journal of Solids and Structures*, 42:338–343, 2012.

[32] Valentine Rey, Guillaume Anciaux, and Jean-François Molinari. Normal adhesive contact on rough surfaces: efficient algorithm for fft-based bem resolution. *Computational Mechanics*, 60(1):69–81, 2017.

[33] H. M. Stanley and T. Kato. An FFT-based method for rough surface contact. *Journal of Tribology*, 119:481–485, 1997.

[34] A. L. Teckentrup, R. Scheichl, M. B. Giles, and E. Ullmann. Further analysis of multilevel Monte Carlo methods for elliptic PDEs with random coefficients. *Numer. Math.*, 125(3):569–600, 2013.

[35] D Wang, A Ueckermann, A Schacht, M Oeser, B Steinauer, and BNJ Persson. Tire–road contact stiffness. *Tribology letters*, 56(2):397–402, 2014.

[36] H. M. Westergaard. Bearing pressures and cracks. *Journal of Applied Mechanics*, 6:49–53, 1937.

[37] Peter Wriggers. *Computational contact mechanics*. Springer Science & Business Media, 2006.

[38] Vladislav A. Yastrebov, Guillaume Anciaux, and Jean-François Molinari. From infinitesimal to full contact between rough surfaces: Evolution of the contact area. *International Journal of Solids and Structures*, 52:83 – 102, 2015.

Recent publications:

INSTITUTE of MATHEMATICS
MATHICSE Group

Ecole Polytechnique Fédérale (EPFL)

CH-1015 Lausanne

2018

01.2018 ANA SUSNAJARA, DANIEL KRESSNER:
A fast spectral divide-and-conquer method for banded matrices

02.2018 ELEONORA ARNONE, LAURA AZZIMONTI, FABIO NOBILE, LAURA M. SANGALLI:
Modelling spatially dependent functional data via regression with differential regularization

03.2018 NICCOLO DAL SANTO, SIMONE DEPARIS, ANDREA MANZONI, ALFIO QUARTERONI:
Mutli space reduced basis preconditioners for parametrized Stokes equations

04.2018 MATTHIEU MARTIN, SEBASTIAN KRUMSCHEID, FABIO NOBILE:
Mutli space reduced basis preconditioners for parametrized Stokes equations
Analysis of stochastic gradient methods for PDE-Constrained optimal control problems with uncertain parameters

05.2018 VALENTINE REY, SEBASTIAN KRUMSCHEID, FABIO NOBILE:
Quantifying uncertainties in contact mechanics of rough surfaces using the Multilevel Monte Carlo method

***